Ceramics International 51 (2025) 34213–34222

Contents lists available at ScienceDirect

Ceramics International

journal homepage: www.elsevier.com/locate/ceramint

# Microstructural optimizations of an iron-containing electrode for electrochemical ammonia synthesis on a proton-conducting ceramic membrane

Philipp Blanck [a,b], Daniel Schmider [b], Robert J. Kee [c], Julian Dailly [b,*], Olaf Deutschmann [a]

[a] Karlsruhe Institute of Technology (KIT), Institute for Chemical Technology and Polymer Chemistry (ITCP), Engesserstr. 20, Karlsruhe, 76131, Germany
[b] European Institute for Energy Research (EIfER), Emmy-Noether-Str. 11, Karlsruhe, 76131, Germany
[c] Colorado School of Mines (CSM), Department of Mechanical Engineering, 1500 Illinois St., Golden, 80401, USA

ARTICLE INFO

*Keywords:*
Proton-conducting ceramic electrolysis cell (PCEC)
Electrochemical ammonia synthesis
PCC manufacturing
Electrode design
Iron catalyst

ABSTRACT

In this study, we address the challenges associated with developing a mechanically and chemically stable electrode featuring iron as the active component for ammonia synthesis. Our investigations reveal that Fe-BCZY721 cermet electrodes induce significant morphological changes in the BCZY721 electrolyte. These changes are influenced by various parameters, such as sintering temperature and the $Fe_2O_3$/BCZY721 ratio, leading to the formation of interlacing Ba-rich and Ce-rich phases. This process is challenging to control and can result in mechanical weakening of the material. As a promising alternative, an iron-filled backbone electrode was proposed, constructed from two consecutively sintered components. In this novel electrode design approach, a porous BCZY721 backbone is first sintered on the electrolyte, followed by incorporation of the catalyst ink into it using a screen-printing technique. This method enables a substantially lower sintering temperature for the catalyst compared to conventional composite electrodes, effectively mitigating morphological alterations while enhancing mechanical stability. Additionally, sintering the scaffold separately from the inserted catalyst provides greater flexibility in adjusting parameters and allows for the introduction of various catalysts as needed. Initial tests demonstrate that the developed electrode design is suitable for ammonia production when compared to existing literature, with ammonia formation rates at −1.2 V against OCV of $1.1{\cdot}10^{-9}$ mol cm$^{-2}$ s$^{-1}$, $4.9{\cdot}10^{-9}$ mol cm$^{-2}$ s$^{-1}$ and $5.0{\cdot}10^{-9}$ mol cm$^{-2}$ s$^{-1}$ measured at 400 °C, 500 °C and 600 °C respectively. The active cell surface area was 12.57 cm$^2$, which is the largest to date in electrochemical ammonia synthesis using proton-conducting ceramic cells.

## 1. Introduction

In 2020, global ammonia production surpassed 185 million tons, with a projected demand increase of 37 % by 2050, excluding its potential use as an energy carrier [1]. According to the International Energy Agency (IEA) 2021 report, ammonia is the most energy-intensive chemical produced globally [2]. The synthesis of ammonia consumes approximately 20 % of the energy used in the broader chemical sector and constitutes 2 % of the total final energy consumption globally. This significant energy demand results in substantial carbon emissions, contributing to 1.3 % of global anthropogenic $CO_2$ emissions. In 2020, producing one ton of ammonia generated an average of 2.4 tons of $CO_2$ [1,2].

Due to its high gravimetric hydrogen density of 17.75 wt%, ammonia is considered as a promising clean energy carrier for chemical energy storage applications. In its liquid state it boasts a comparatively high volumetric energy density of 3.2 kW h L$^{-1}$ at −33 °C and atmospheric pressure, surpassing that of liquid hydrogen at −253 °C (2.4 kW h L$^{-1}$) and compressed hydrogen at 1000 bar (1.7 kW h L$^{-1}$). At 20 °C, ammonia can be stored in liquid form under a pressure of 8.58 bar, and storage at atmospheric pressure is achievable by cooling to −33 °C. Currently, iso-thermal tanks with a capacity of 45 000 tons of ammonia represent the state of the art [3].

The conventional method for ammonia production is the Haber–Bosch process, which requires harsh reaction conditions, typically operating at pressures of 20 MPa to 40 MPa and temperatures between 400 °C and 500 °C, due to its inherent thermodynamic and kinetic constraints. Recent advancements have concentrated on the development of proton-conducting ceramic electrolysis cells (PCECs) as a means to enable sustainable ammonia synthesis [4]. However, the strong triple bond

* Corresponding author.
*E-mail addresses:* julian.dailly@eifer.org, Dailly@eifer.org (J. Dailly).

https://doi.org/10.1016/j.ceramint.2025.05.149
Received 6 February 2025; Received in revised form 7 April 2025; Accepted 11 May 2025
Available online 2 June 2025

**Table 1**
Overview of electrode materials used for electrochemical ammonia synthesis in literature.

| Active ammonia electrode | Reference |
|---|---|
| Pure metal electrodes: | |
| iron (Fe) | [9–12] |
| iron-palladium (Fe-Pd) | [12] |
| iron-ruthenium (Fe-Ru) | [12] |
| palladium (Pd) | [13,14] |
| silver (Ag) | [15] |
| platinum (Pt) | [15] |
| rhodium (Rh) | [16] |
| silver-palladium (Ag-Pd) | [17–28] |
| Cermet and oxide electrodes: | |
| $Fe\text{-}BaZr_{0.8}Ce_{0.2}O_3$ | [9] |
| $BaZr_{0.5}Fe_{0.4}Y_{0.1}O_3$ | [9] |
| $Fe\text{-}BaCe_{0.9}Y_{0.1}O_3$ | [10] |
| $W\text{-}Fe\text{-}BaCe_{0.9}Y_{0.1}O_3$ | [10] |
| $Ni\text{-}BaCe_{0.8}Y_{0.1}Ru_{0.1}O_{3-\delta}$ | [29] |
| $Ni\text{-}BaCe_{0.9}Y_{0.1}O_{3-\delta}$ | [29] |
| $Ba_{0.5}Sr_{0.5}Co_{0.8}Fe_{0.2}O_{3-\alpha}$ | [24] |
| $Ni\text{-}BaZr_{0.8}Y_{0.2}O_{3-\delta}$ | [30] |
| $Fe\text{-}BZr_{0.8}Y_{0.2}O_{3-\delta}$ | [31] |
| $Ni\text{-}BaZr_{0.7}Ce_{0.2}Y_{0.1}O_{2.9}$ | [32] |
| $La_{0.5}Sr_{0.5}Ti_{0.6}Ru_{0.4}O_3$ | [18] |
| $La_{0.6}Sr_{0.4}Co_{0.2}Fe_{0.8}O_{3-\delta}$ | [15] |
| $La_{0.8}Cs_{0.2}Fe_{0.8}Ni_{0.2}O_{3-\delta}$ | [33] |
| $Pr_{0.6}Ba_{0.4}Fe_{0.8}Cu_{0.2}O_{3-\delta}$ | [34] |
| $Sm_{0.6}Ba_{0.4}Fe_{0.8}Cu_{0.2}O_{3-\delta}$ | [35] |
| $La_{0.6}Sr_{0.4}Co_{0.2}Fe_{0.8}O_{3-\delta}\text{-}Ce_{0.8}Gd_{0.18}Ca_{0.02}O_{2-\delta}$ | [36] |
| $La_{0.6}Sr_{0.4}FeO_{3-\delta}\text{-}Ce_{0.8}Gd_{0.18}Ca_{0.02}O_{2-\delta}$ | [36] |
| $Sr_xTi_{0.6}Fe_{0.4}O_{3-\delta}$ | [37] |
| $La_{0.75}Sr_{0.25}Cr_{0.5}Fe_{0.5}O_{3-\delta}\text{-}Ce_{0.8}Gd_{0.18}Ca_{0.02}O_{2-\delta}$ | [38] |
| $LaCu_{0.1}Fe_{0.9}O_{3-\delta}$ | [39] |
| $Ru/La_{0.25}Ce_{0.75}O_{2-x}$ | [40] |

in nitrogen (N≡N dissociation energy: 941 kJ $mol^{-1}$) presents a considerable hurdle due to chemical activation. This challenge, combined with the occurrence of rapid side reactions, leads to ammonia production efficiencies, that are currently insufficient for practical applications. Consequently, further advancements are necessary to improve the overall efficiency of the process. The United States Department of Energy (DOE) has established benchmarks for the commercialization of this emerging technology, specifying an ammonia production rate $r_{NH_3}$ ~$10^{-6}$ mol $cm^{-2}$ $s^{-1}$, a current density $j$ >300 mA $cm^{-2}$, and a Faraday efficiency $\eta_{NH_3}$ of 90 % [5].

In the Haber–Bosch process, ammonia production using the KM1 catalyst yields approximately $10^{-5}$ to $10^{-6}$ mol $g^{-1}$ $s^{-1}$ of ammonia [6,7]. When converting this to the surface area of the reduced KM1 catalyst, it translates to around $10^{-10}$ mol $cm^{-2}$ $s^{-1}$, with an ammonia outlet concentration up to 10 %, depending on the gas flow rate [7,8]. However, this figure is not directly comparable to the electrochemical ammonia production route, as the calculation for the latter typically considers the plain geometric surface area of the electrode rather than the accessible surface area of the porous structure within the electrode.

The electrochemical reduction of nitrogen ($N_2$) to ammonia ($NH_3$) at elevated temperatures ranging from 400 °C to 600 °C has been explored using a variety of catalysts so far. The catalysts used for ammonia synthesis, including both metal and cermet electrodes, are summarized in Table 1 for a clear and concise overview.

Precious metal, cermet, and oxide electrodes have demonstrated similar ammonia formation rates, up to approximately $10^{-9}$ mol $cm^{-2}$ $s^{-1}$. However, recent studies indicate that using non-precious iron as an electrocatalyst can achieve production rates on the order of $10^{-8}$ mol $cm^{-2}$ $s^{-1}$, although with relatively low Faradaic efficiencies [9,30,41]. This represents a significant advancement towards meeting the benchmarks for commercial viability. However, significant improvements are still necessary to achieve the targets set by the DOE.

As shown in Table 1, various electrode compositions for electrochemical ammonia synthesis have been developed. The first part of the table presents configurations of purely metallic catalysts applied directly to the cell membrane, while the second part highlights catalysts premixed with a ceramic component and co-sintered to form a catalytically active porous electrode, as well as pure oxides exhibiting both electronic and ionic conductivities (MIEC).

In this study a novel electrode design and processing method was developed, featuring a porous $BaCe_{0.7}Zr_{0.2}Y_{0.1}O_{3-\delta}$ (BCZY721) backbone that serves as a scaffold for the subsequent pressing-in of a low-viscosity $Fe_2O_3$-based ink. This backbone-based in-pressed structure has not been studied in the literature before. The advantage of this design lies in the two-step sintering process, where each component of the electrode is sintered separately, allowing for better control over the microstructure and distribution of the active material. This technique yielded a homogeneous distribution of iron particles across the extensive surface area of the ceramic backbone. Additionally, this method enables precise dosing and application of the active material per unit area. The resulting electrode exhibits several promising properties, including enhanced mechanical stability, a large surface area, and a uniform distribution of iron particles over an active cell area of 12.57 $cm^2$. These characteristics show that the electrode design is well-suited for applications requiring high active surface area and robust structural integrity.

## 2. Experimental

### 2.1. Powders

All powders used in this study are commercially available. The anode and electrolyte layers were fabricated using $BaCe_{0.8}Zr_{0.1}Y_{0.1}O_{3-\delta}$ (BCZY811) and $BaCe_{0.7}Zr_{0.2}Y_{0.1}O_{3-\delta}$ (BCZY721) sourced from CerPoTech AS, along with NiO from JT Baker® and ZnO from Sigma Aldrich.

The cathode components comprise $BaCe_{0.7}Zr_{0.2}Y_{0.1}O_{3-\delta}$, also supplied by CerPoTech AS, $\alpha$-Fe(III)-oxide powder (30 nm to 50 nm, 98 % metal basis and <5 μm, 96 % metal basis) obtained from Merck, and TIMREX SFG75 Graphite provided by TIMCAL.

### 2.2. Cell fabrication

#### 2.2.1. Anode

The anode support was fabricated via a tape-casting process. The anode slurry consisted of a mixture of NiO/BCZY811 in a ratio of 1.5/1 (w/w), graphite as a pore former, a dispersing agent (Nuosperse), and solvents (butanone/ ethanol). This mixture was homogenized using a Turbula® type T2F mixer (WAB) for 24 h. Subsequently, a binder (Polyvinyl butyral) and plasticizers (PEG/TEG-EH by Eastman) were incorporated, and the resulting mixture was further milled for three hours. This was followed by a resting period of 24 h. The final preparation step involved de-airing the slurry under vacuum for 10 min to remove entrapped air bubbles. The prepared slurry was then casted using a ZAA 2300 automatic film applicator coater (Zehntner GmbH) onto a glass plate covered with a polymer sheet. The resulting anode tape was dried at room temperature for 24 h, resulting in a final thickness of 500 μm. Finally, circular samples with a diameter of 77 mm were cut from the tape for further processing.

#### 2.2.2. Electrolyte

The BCZY721 powder was blended with a carrier mixture ($\alpha$-terpineol and ethyl cellulose) and zinc oxide (0.5 wt.%) as a sintering aid. This mixture was first ground in an automatic mortar (Retsch RM200) for 20 min, and the resulting slurry was then further processed using a roller mill to break up any remaining agglomerates. The prepared electrolyte ink was applied to the green tape cut-outs via screen-printing using an EKRA E2 screen-printer. Subsequently, the

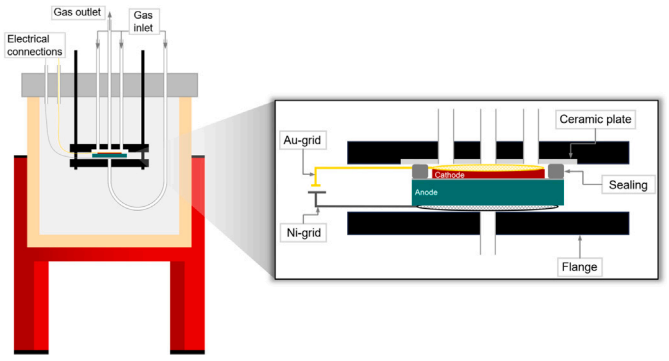


**Fig. 1.** Schematic representation of the double flange setup with a more detailed view of the cell assembly.

half-cell was stored at room temperature for at least 1 h to ensure complete drying, followed by co-sintering at 1400 °C for 8 h. The sintering process included specific dwelling steps, intended for solvent evaporation at 250 °C and burning of graphite from the anode tape at 550 °C. These steps were critical to achieving a dense and defect-free electrolyte film, ensuring optimal ionic conductivity and mechanical integrity of the cell structure.

#### 2.2.3. Cathode

In an initial attempt at fabricating a Fe-BCZY composite electrode, $Fe_2O_3$ was directly blended with BCZY721 powder, along with a vehicle and carbon, to form the cathode layer. This cermet was applied to the half cell by screen-printing. The solid loading was consistently maintained at 45 % by weight, with a BCZY721/graphite ratio of about 1.5:1 (w/w). The ratio of $Fe_2O_3$ to BCZY721 was varied between 0.25:1 and 2:1 (w/w). Sintering temperatures ranging from 1000 °C to 1300 °C were evaluated for the consolidation of the cermet electrodes.

In a second approach, the cathode was applied to the sintered half-cell by screen-printing a porous BCZY721 backbone. Then the ink containing the catalyst was applied through "screen-pressing", i.e. using screen-printing to impress the ink into the porous, previously sintered layer. The catalyst ink was then sintered separately.

The first layer comprised a backbone of BCZY721 mixed with graphite in a 1.5:1 (w/w) ratio, dispersed in a vehicle composed of $\alpha$-terpineol and ethyl cellulose. The solid content of the backbone ink was maintained at 45 % by weight. After applying the backbone layer to the half-cell, it was dried in a drying cabinet under ambient air conditions until the color changed from glossy to matte, indicating adequate drying. Subsequently, the dried layer was sintered at 1350 °C for 1 h, with controlled heating and cooling ramps of 3 K $min^{-1}$. This sintering process ensured the formation of a well-adhered and structurally stable backbone layer, providing a suitable scaffold for the subsequent deposition of the functional cathode layer.

In the following step, the catalytically active part of the cathode was applied. $Fe_2O_3$ powder was mixed with graphite and the same carrier mixture used for the electrolyte. To ensure optimal distribution of the iron particles within the cathode's backbone, the low-viscosity iron ink was carefully "screen-pressed" into the backbone using the screen-printing process. After the application, the iron layer was dried at room temperature and ambient air conditions. To increase the total amount of available catalyst, additional layers of iron ink were sequentially applied, with drying steps between each application. Following this drying period, the cell was calcined at 850 °C for 1 h, with controlled heating and cooling ramps of 3 K $min^{-1}$. The completed protonic ceramic cell with a diameter of 52 mm features a total surface area of 21.24 $cm^2$ and an active surface area of 12.57 $cm^2$ at a diameter of 40 mm.

### 2.3. Electrochemical and structural characterization

For electrochemical characterization, the completed PCC is then tested in a double-flange test stand lined with aluminum oxide (Fiaxell SOFC Technologies™). Electrical contact to the NiO-BCZY811 electrode support is provided by Inconel 600 and nickel wires (⌀ 0.5 mm) connected to a nickel foam (⌀ 50 mm) and via gold wires (⌀ 0.5 mm) connected with a gold grid (⌀ 40 mm) to the Fe-BCZY721 electrode. A detailed schematic diagram of the assembled cell is shown in Fig. 1.

Prior to assembling the test housing, the cell is sealed with a sodium-silicate, aluminum oxide-based gas-tight sealing agent. Currently, no commercially available sealing solutions for PCCs exist, and research in this field is ongoing, with promising results achieved using the above mentioned materials [42]. This sealing agent is applied in thin layers and allowed to dry at room temperature for 4 h before the other components are assembled and attached to the cell. After complete assembly, the cell housing is placed in a top-loader Squadro SQ11 (Kittec) furnace and is heated to 600 °C with a heating rate of 1 K $min^{-1}$ while 2 $NLh^{-1}$ $N_2$ is supplied to both electrodes. Additionally, dwell times of 2 h at 100 °C, 260 °C and 650 °C are implemented during the start-up phase to cure the seal.

The gas composition was regulated using mass flow controllers (Bronkhorst), with the respective gases mixed immediately after exiting the controllers before being introduced into the test stand.

The Electrochemical Impedance Spectroscopy (EIS) measurements were performed using a Zahner Zennium (Zahner) instrument. The frequency range was set between 100 kHz and 100 mHz, with an AC amplitude set to 15 mV, measured at open circuit voltage (OCV) under a symmetric gas environment.

The scanning electron microscopy (SEM) analysis was performed using an FEI Quanta 200 electron microscope. The cells were manually fractured and mounted onto a sample carrier. The samples were then analyzed in an ultra-high vacuum environment with an acceleration voltage of 15 kV. The working distance between the sample and the objective lens was set to approximately 10 mm.

A high-angle annular dark field detector (HAADF) in X-ray spectroscopy, operating in scanning transmission mode (STEM-EDXS), was used to detect the element distribution in a cross-sectional image of the cell.

The topographical investigations were carried out with the non-contact profilometer cyberSCAN CT 300 (cyberTechnologies) including the company's own automation software SCAN SUITE.

Ammonia formation was detected using a high performance ion-selective electrode from Thermo Scientific™ (Orion™ 9512HPBNWP). For each applied voltage and temperature, the downstream gas was fed through a 0.01 mol $L^{-1}$ $H_2SO_4$ solution for 20 min to trap the ammonia. based on promising conditions reported in the literature, a $H_2$:$N_2$ ratio of 1 with a gas flow rate of 20 $NLh^{-1}$ was used.

## 3. Results and discussion

### 3.1. Cell structure and morphology

#### 3.1.1. Fe-BCZY721 cermets

During the initial development of the ammonia electrode, a test matrix was established, wherein $Fe_2O_3$/BCZY721 mixtures were prepared in ratios ranging from 0.25:1 to 2:1 (w/w) and applied directly to the half-cell by screen-printing. Each ink was then sintered at different temperatures to find the optimal sintering conditions. At temperatures that were too low, delamination and unsintered particles were observed. At temperatures that were too high, the cermet melted on the electrolyte. It was determined that mixtures of BCZY721 and $Fe_2O_3$ in an approximately 1:1 (w/w) ratio require temperatures exceeding 1200 °C for sufficient sintering, preventing delamination and unsintered particles. Lower sintering temperatures can be used with increasing

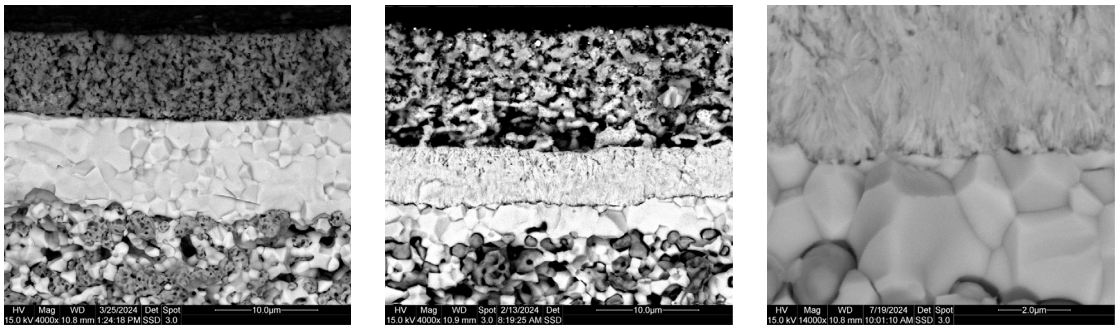


**Fig. 2.** (a): Cell with NiO-BCZY811 (bottom) support electrode and BCZY721 electrolyte (light) to show an unaffected electrolyte without changes during sintering for comparison. The upper electrode is not relevant for this study other than it not affecting the electrolyte during sintering. (b): The top layer represents the BCZY721-$Fe_2O_3$ cermet electrode, the middle layer is the BCZY721 electrolyte exhibiting a prominent crack at its center separating two different morphologies of the electrolyte, and the bottom layer corresponds to the NiO-BCZY811 supporting electrode. (c): A magnified view of the formed demarcation in the electrolyte as also shown in (b).

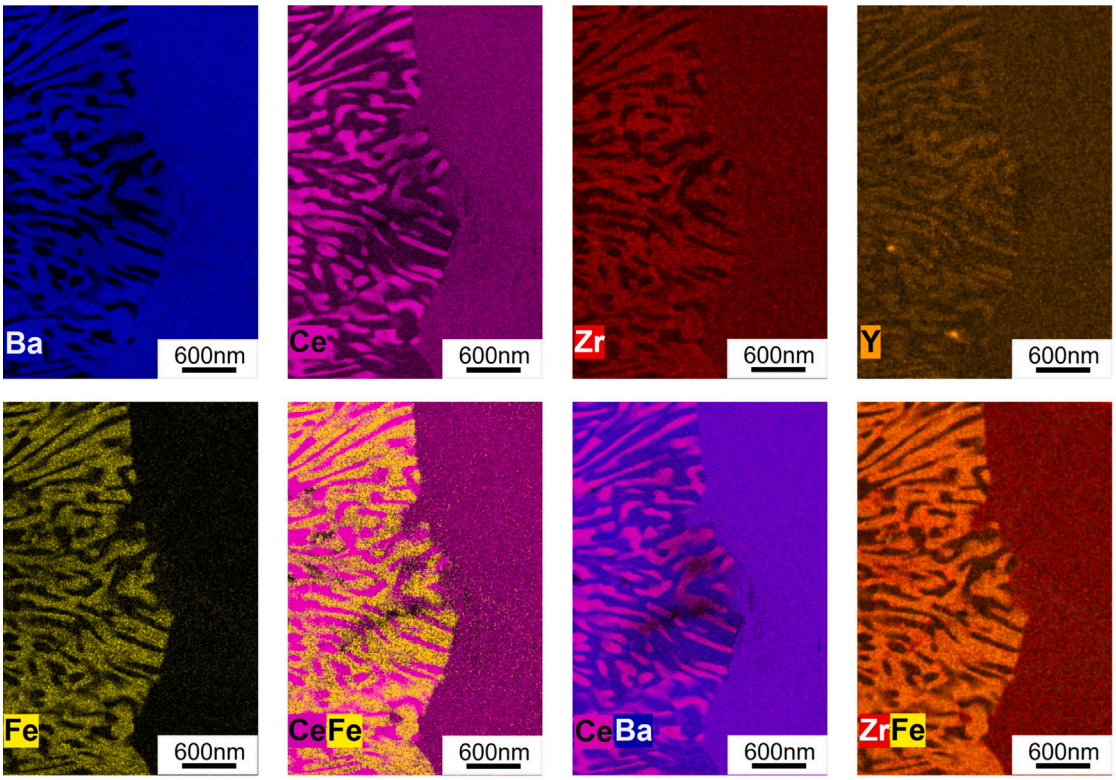


**Fig. 3.** STEM-EDXS images taken in the same region at the demarcation in the electrolyte up to which the morphological changes occur after sintering of a Fe-BCZY721 cermet cathode (compare Fig. 2(c)). The analysis focuses on the distribution of Ba, Ce, Zr, Y, Fe and Ni. All eight images show the same section of the electrolyte, with the respective focus on different elements. Left side (lamellar pattern): Morphological changes at the interface with the Fe-BCZY721 cermet electrode, the cathode. Right side (uniform): Unchanged electrolyte towards the NiO-BCZY811 supporting electrode, the anode.

$Fe_2O_3$ content, but not below 1000 °C for a $Fe_2O_3$/BCZY721 ratio of 2:1 (w/w).

At increasing sintering temperatures of $Fe_2O_3$-BCZY721 mixtures, morphological changes in the structure of the Fe-containing electrode and in the adjacent electrolyte were observed, as can be seen in Figs. 2(b) and 2(c) (for a direct comparison with an intact electrolyte, see Fig. 2(a)). As the sintering temperature increases, the border between the emerging lamellar pattern and the unaltered electrolyte moves progressively towards the supporting electrode. High sintering temperatures were mandatory for mixtures with a low Fe content to ensure proper sintering, which led to observable structural changes that extended far into the support anode. By increasing the $Fe_2O_3$/BCZY721 ratio to 2:1, the sintering temperature could be significantly reduced. But even at temperatures around 1000 °C, microstructural changes that affected the electrolyte over several micrometers were still observed.

This morphological change, in some cases, led to the formation of a sharp crack in the center of the electrolyte, significantly compromising mechanical stability and resulting in full or partial delamination of the ammonia electrode after cell reduction. Another drawback of the Fe-BCZY721 cermets is the high ohmic and polarization resistances observed during electrochemical impedance measurements. This issue can be attributed to the formation of the lamellar interfacial layer, which was also observed within the porous structure of the ammonia electrode and causes high interfacial contact resistance. This layer likely acts as a isolating phase for both electrons and protons, thereby significantly reducing or completely obstructing the cell's conductivity.

In 2022, Okazaki et al. revealed that the interfacial layer formed between a Fe-BZY composite or pure Fe and a BCY electrolyte primarily consists of ceria, with possible doping of Ba and Fe [9]. It was also observed that the interfacial layer appeared exclusively in cells with Fe or Fe-BZY electrodes, which demonstrated higher ammonia formation rates. This finding suggests that the interfacial layer may significantly contribute to the electrochemical promotion of ammonia synthesis. However, in 2024, Okazaki et al. tested electrodes fabricated from various ratios of $CeO_2$:$Fe_2O_3$ with the aim of targeting the formation of the interfacial layer as an active site for ammonia production [41]. It was revealed that single-chamber ammonia electrosynthesis using ceria-iron electrodes resulted in ammonia formation rates comparable to those achieved with pure iron electrodes of $1.2{\cdot}10^{-8}$ mol cm$^{-2}$ s$^{-1}$ at 600 °C.

To provide a detailed representation of the morphological changes occurring in the BCZY721 electrolyte with the Fe-BCZY721 cermet electrode, especially the composition of the lamellar pattern, additional characterization was conducted using STEM-EDXS (X-ray spectroscopy in scanning transmission mode) mapping measurements. Fig. 3 displays the elemental distribution directly along the demarcation in the middle of the electrolyte, which is also presented in Fig. 2. The resulting interlacing layers are present throughout the entire ammonia electrode. This pattern was also observed in the support electrode when sintering at elevated temperatures.

From Fig. 3, it is evident that segregation occurs within the electrolyte adjacent to the Fe-containing cermet electrode. Two distinct but abutting phases can be observed: one that is Ba-rich and another that is Ce-rich. The Ba-rich phase also exhibits an enrichment of Fe and Zr, while the Ce-rich phase shows an enrichment of Y. The clear demarcation of these elements suggests the formation of a Ce + Y phase and a Fe + Ba + Zr phase.

The formation of these two distinct phases is primarily driven by the specific chemical properties and interactions of the elements during sintering, as well as the structural and thermodynamic conditions that favor phase separation. According to our observations, in particular the temperature plays a decisive role in the propagation of the morphological changes. Due to the complexity and the numerous parameters involved in forming these phases, controlling the resultant morphological changes becomes challenging. Consequently, the long-term stability, interactions, and other critical factors have not yet been thoroughly investigated. Given these challenges, an electrode design where the active material (Fe) is sintered together with the ceramic component is no longer a viable option, especially with the frequent occurrence of ammonia electrode delamination observed after the reduction of the cell. As a result, this study shifted focus toward developing an electrode design where the relevant parameters can be more effectively controlled, ensuring better performance and stability.

### 3.1.2. Iron-filled backbone design

For the development of an effective cathode design for electrochemical ammonia synthesis, several critical properties of the ammonia electrode must be considered, including mechanical stability, strong adhesion to the electrolyte, a percolating electrically conductive phase, high surface area, and uniform distribution of the catalytically active material. Iron was selected as the active material because it has demonstrated superior performance in the literature compared to noble metal catalysts [9,10,30]. Furthermore, iron is promising for ammonia synthesis due to its high binding energy with nitrogen [43]. The resulting cell structure, which was produced as described 2.2.3, is depicted in its oxidized state in Fig. 4. The images, captured using secondary electron (SE) and backscattered electron (BSE) detectors on a scanning electron microscope (SEM) reveal a percolating layer of iron on the pre-applied backbone with particle diameters ranging from 50 nm to 250 nm, with an average of around 210 nm.

Furthermore, no morphological changes were observed in the backbone or the electrolyte of the cell. This chemical stability is primarily attributed to the low-temperature sintering of the pure iron ink, which was pressed into the backbone and then sintered separately at 850 °C.

However, increasing the thickness of the supporting backbone layer beyond 20 µm made it increasingly difficult to achieve uniform distribution of the $Fe_2O_3$-ink in the porous layer throughout the depth of the backbone. Insufficient penetration of the iron ink led to the formation of a non-percolating catalyst layer, compromising the catalytic efficiency. A backbone thickness of approximately 15 µm to 20 µm was found to facilitate proper distribution of the low-viscosity $Fe_2O_3$-ink, ensuring the formation of a well-percolated catalyst up to the electrolyte layer. To further increase the total catalyst loading on the

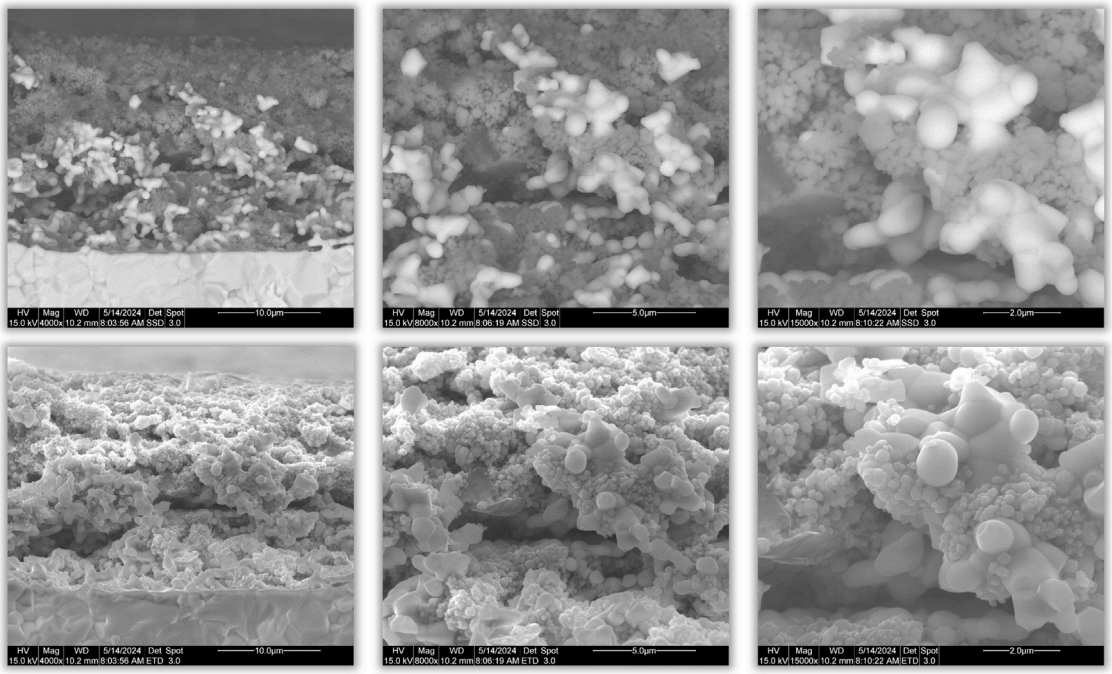

**Fig. 4.** SEM image with BSE (top) and SE (bottom) detector of an $Fe_2O_3$-ink (dark phase) pressed into a backbone (bright phase) electrode in the oxidized state.

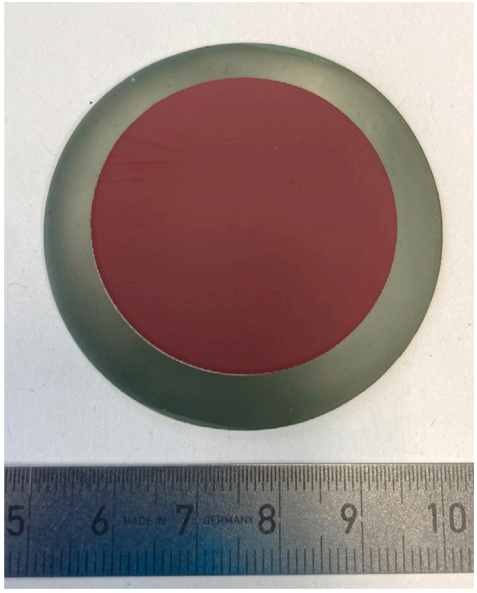


**Fig. 5.** Top view of the final cell design with a diameter for 52 mm, consisting of a BCZY811 support electrode, a BCZY721 electrolyte layer, and a iron-filled backbone electrode.

ammonia electrode, additional layers of $Fe_2O_3$-ink were applied to the electrode surface using screen-printing. These additional catalyst layers demonstrated strong adhesion to the underlying backbone, resulting in a thicker, porous catalyst layer on the top that should substantially enhance the available catalytic surface area.

### 3.2. Topographical investigations

With increasing cell sizes (>20 $cm^2$ in this work) the challenges regarding flatness are becoming more significant and as a anticipatory characterization the macroscopic shape of the cell was analyzed topographically. A top view of the fabricated proton-conducting ceramic cell with the iron-filled backbone ammonia electrode attached can be seen in Fig. 5.

The results of the topographic investigations, see Fig. 6, show that the cell exhibits a convex curvature in the direction of the ammonia electrode, a feature that is much less pronounced in topographical studies of the half-cell only. This amplified curvature is probably a result of the sintering process of the backbone onto the half-cell at 1350 °C. The apex of the curvature extends about half a millimeter beyond the edge of the round cell, which becomes particularly clear when looking at the topography of the supporting electrode side of the cell. However, the images demonstrate that the curvature of the front and back sides match and that the cell thickness remains uniform. Despite the cell's slight deviation from perfect flatness, its inherent flexibility enabled seamless screen-printing, "screen-pressing", sealing, and testing without any complications. As the cell size is further scaled up, minor curvature becomes even less critical, as larger cells exhibit increased flexibility.

### 3.3. Electrochemical characterization

For the electrochemical characterization of the cells, EIS (Electrochemical Impedance Spectroscopy) measurements were conducted at OCV (Open Circuit Voltage). Fig. 7 presents Nyquist plots for the two configurations: the Fe-BCZY721 cermet with additional platinum current collector (a) and the iron-filled backbone electrode (b). In both configurations, the supporting electrode was a Ni-BCZY811 cermet, and the electrolyte thickness was in the same range between 8 µm to 9 µm.

**Table 2**
Electrochemical Comparison between premixed Fe-BCZY721 cermet electrode with Pt-current collector (a) and the iron-filled BCZY721-backbone assembly (b) fitted by the equivalent circuit model presented in Fig. 8.

| Cell | $T$/°C | $ASR_{ohm}$/Ω $cm^2$ | $ASR_{pol}$/Ω $cm^2$ | $ASR_{tot}$ / Ω $cm^2$ |
|---|---|---|---|---|
| (a) | 400 | 14.20 | 80.20 | 94.40 |
| (a) | 500 | 7.18 | 42.22 | 49.40 |
| (a) | 600 | 4.14 | 13.54 | 17.67 |
| (b) | 400 | 4.15 | 7.58 | 11.73 |
| (b) | 500 | 2.30 | 4.79 | 7.09 |
| (b) | 600 | 1.85 | 2.41 | 4.26 |

It is evident that the iron-filled BCZY721-backbone assembly exhibits lower ohmic resistance, polarization resistance, and, consequently, a reduced total resistance compared to the Fe-BCZY721 cermet electrode. The increased resistances of the Fe-BCZY721 cermet electrode, as shown in Fig. 7, may be attributed to the formation of the lamellar pattern. Specifically, the interface contact resistance, influenced by all those boundaries of the lamellar pattern, is expected to have a significant impact on both ohmic and polarization resistance.

The measured impedance spectra were analyzed and fitted using an equivalent circuit model, as illustrated in Fig. 8, employing Zahner Analysis software.

The model comprises several key components: an inductance ($L_0$), which accounts for the inductive effects often caused by wiring or connections; an ohmic resistance ($R_0$), representing the inherent resistance of the electrolyte or other materials in the system; and two resistor-constant phase element (R-CPE) components. These R-CPE components model the non-ideal capacitive behavior of the electric double layer at the electrode/electrolyte interface and charge transfer processes within the system. The CPE accounts for deviations from ideal capacitor behavior due to surface roughness, inhomogeneities, or other factors. Effects of mass transfer limitations, such as diffusion of reactants and products may also be modeled with R-CPE elements.

The specific resistance values are detailed in Table 2 and were fitted by the equivalent circuit model presented in Fig. 8 for both types of electrodes described in Section 3.

The total fitting error for the impedance spectra remained consistently below 1.5 % for both cell configurations and all temperatures tested. In addition, the phase angle error was consistently kept below 0.05°, indicating a high degree of accuracy in fitting the impedance data. In addition to modeling and fitting with the equivalent circuit shown in Fig. 8, a modified model incorporating an additional R-CPE element was also tested against the impedance data. However, the results indicate that with resistance values below 1 mΩ, along with the significance level of the third R-CPE element being less than 0.01, can be disregarded. Moreover, the overall fitting error did not improve. Therefore, the equivalent circuit presented in Fig. 8 proves to be the most suitable and meets the required criteria.

### 3.4. Ammonia formation

The developed iron-filled backbone electrode design shown in Fig. 4 was then tested and mounted in the double-flange setup displayed in Fig. 1. The experimental settings were selected based on promising conditions reported in the literature, utilizing a $H_2$:$N_2$ ratio of 1:1 with a gas flow rate of 20 $NLh^{-1}$. Fig. 9 presents the results from a test at various polarizations, which yielded promising ammonia formation rates. The rate enhancement ratio $\rho$ (the ratio of the closed-circuit catalytic rate at −1.2 V to the open-circuit catalytic rate) increases from 2.6 to 7.1, and then settled at around 7.0 as the temperature decreases from 600 °C to 500 °C, and subsequently to 400 °C. At a voltage of −1.2 V, ammonia formation rates $r_{NH_3}$ of $1.1 \cdot 10^{-9}$ mol $cm^{-2}$ $s^{-1}$, $4.9 \cdot 10^{-9}$ mol $cm^{-2}$ $s^{-1}$ and $5.0 \cdot 10^{-9}$ mol $cm^{-2}$ $s^{-1}$ were measured at 400 °C, 500 °C and 600 °C, respectively. The Fe-catalyst loading on the 12.57 $cm^2$ active cell area was 4.4 mg $cm^{-2}$.

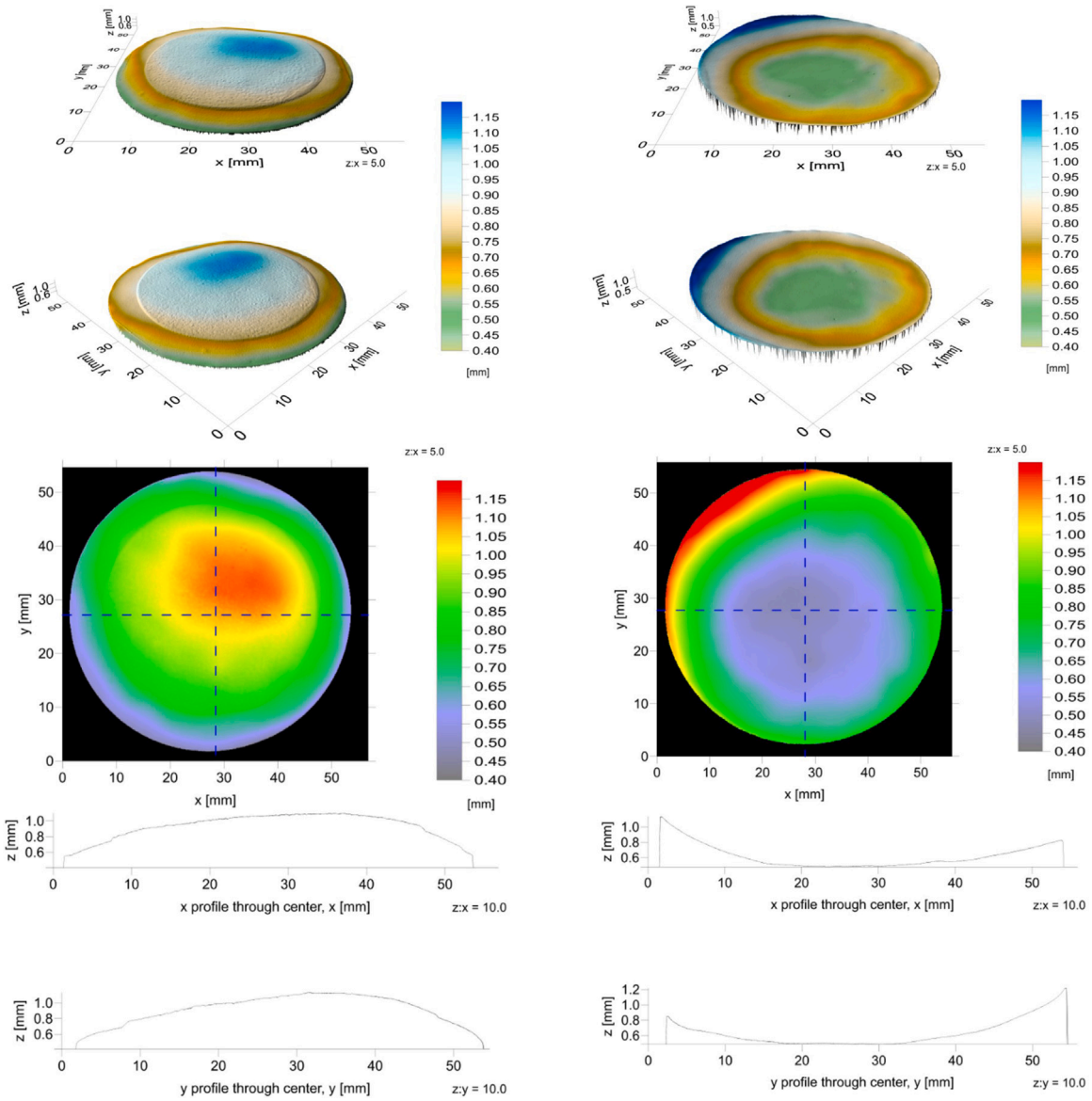


**Fig. 6.** Topographical investigations of cell composed of a NiO-BCZY811 support electrode, a BCZY721 electrolyte and iron-filled backbone. Left side: Top view, highlighting the iron-filled backbone electrode. Right side: View from below, focusing on the NiO-BCZY811 support electrode. Top: 3D visualization with exaggeration to highlight the unevenness, magnified by a factor of 5 to enhanced visual clarity. Middle: Height profile. Bottom: Cross-sectional profile.

The limited increase observed at 600 °C may be attributed to thermodynamic constraints. For fixed operating conditions with a $N_2$:$H_2$ ratio of 1:1 and a volume flow of 20 $NLh^{-1}$, the thermodynamic equilibrium values are $2.7{\cdot}10^{-8}$ $mol\,cm^{-2}\,s^{-1}$, $7.0{\cdot}10^{-9}$ $mol\,cm^{-2}\,s^{-1}$ and $2.4{\cdot}10^{-9}$ $mol\,cm^{-2}\,s^{-1}$ at 400 °C, 500 °C, and 600 °C, respectively. At 600 °C, $NH_3$ formation surpasses the thermodynamic equilibrium value, which can be attributed to the shift in hydrogen partial pressure at the cathode and in the downstream caused by proton pumping and the hydrogen evolution reaction. These elevated $H_2$ partial pressures in the downstream, as well as $H_2$ concentration gradients at the cathode, are not accounted for in the thermodynamic calculations and may contribute to the high ammonia formation rate observed at 600 °C. However, further increases at 600 °C may be restricted by $NH_3$ cracking in the reactor's hot zone. From a thermodynamic perspective, operating at lower temperatures is therefore more favorable. Fig. 9(b) presents the corresponding current densities, from which the electrochemical Faraday efficiencies for ammonia production are derived. The electrochemical Faraday efficiency is calculated as follows:

$$FE_{NH_3} = \frac{nF(r_{NH_3}, j - r_{NH_3,OCV})}{j} \cdot 100 \quad (1)$$

and reaches a peak of 0.53 % at −1.2 V and 500 °C. In this equation, $n$ stands for the number of electrons transferred per molecule of the target product, which is 3 for $NH_3$. $F$ represents the Faraday constant and $j$ the current density applied per $cm^2$ cell area.

To further enhance the ammonia synthesis rate, a thermodynamic approach suggests increasing the volume flow per cell area and reducing the operating temperature. Additionally, increasing the catalyst loading to maximize the number of active sites could prove beneficial. Overall, the achieved ammonia formation rates rank among the highest reported in the literature for electrochemical ammonia synthesis on a PCC with the largest active area of 12.57 $cm^2$ in this field to date.

### 3.5. Post-test microstructural characterization

Fig. 10 shows the cathode microstructure after testing in a reducing atmosphere for over a week. The images reveal that no morphological

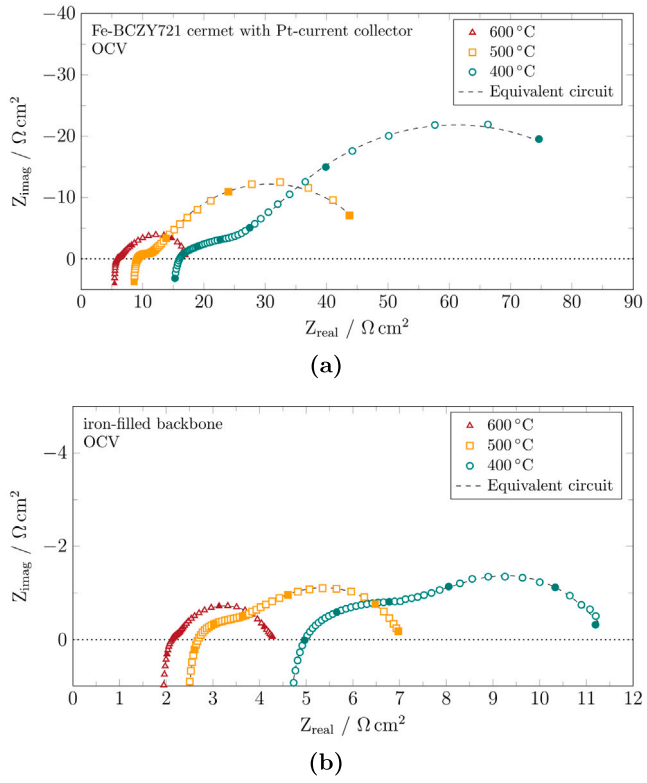


**Fig. 7.** Comparison of the Nyquist plots of the Fe-BCZY721 cermet electrode with Pt-current collector (a) and the iron-filled BCZY721-backbone (b), color-filled circles mark the decades for the frequency range 100 mHz to 100 kHz. The dashed lines show the modeled spectra with the equivalent circuit in Fig. 8.

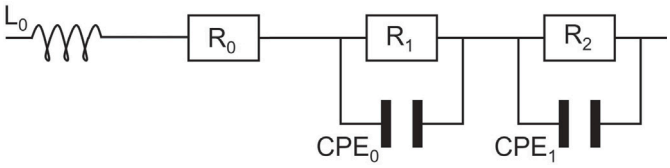


**Fig. 8.** Equivalent circuit for modeling the impedance spectrum.

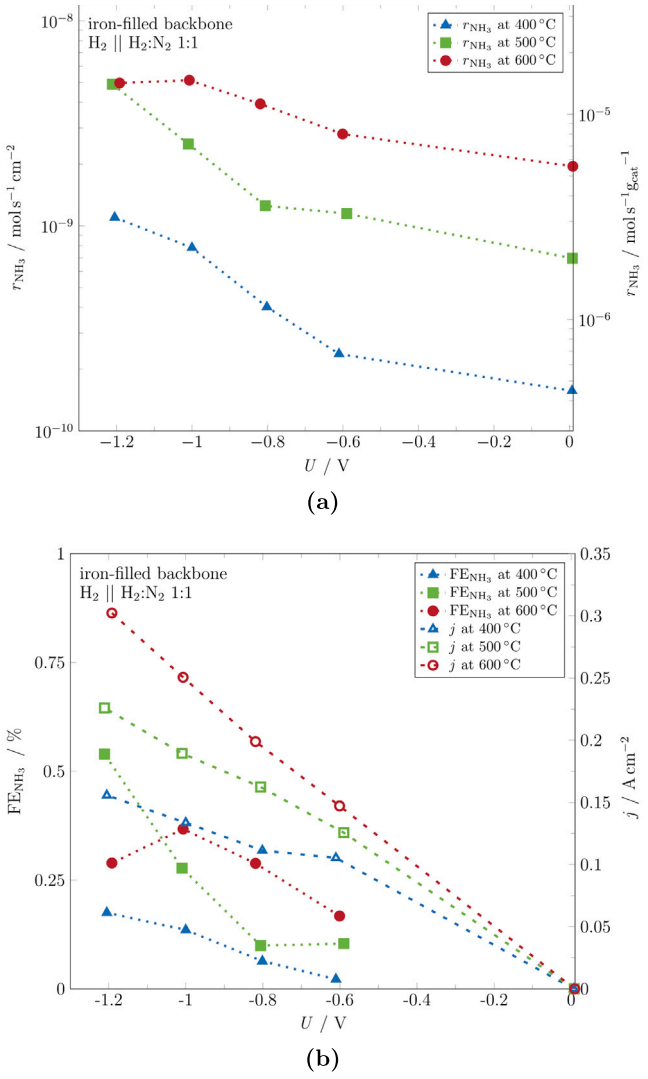


**Fig. 9.** (a): Ammonia formation rates of the iron-filled backbone electrode measured as a function of the applied voltage at 400 °C, 500 °C and 600 °C plotted in relation to the area in cm$^2$ (left axis) and to the catalyst loading (reduced state) in $g_{cat}$ (right axis). The $H_2$:$N_2$ ratio of 1:1 was kept constant with a gas flow rate of 20 NLh$^{-1}$. (b): Electrochemical Faraday efficiency to ammonia, $FE_{NH_3}$, in % (left axis) and corresponding current density at the respective temperature and voltage (right axis).

changes occurred in the ceramic components, the backbone, or the electrolyte. The iron grains remain well distributed within the backbone and are securely attached to the additional iron layer on top of the backbone. In contrast to the initially tested BCZY721-$Fe_2O_3$ cermet electrodes, neither delamination nor surface erosion was observed on the ammonia electrode after reduction and testing. As anticipated, the reduction process resulted in a decrease in particle size. Following the reduction, the average particle size was measured to be approximately 180 nm.

## 4. Conclusions

In this work, we found that developing a mechanically and chemically stable ammonia electrode containing iron as the active component poses significant challenges. The Fe-BCZY721 cermets exhibit morphological changes in the BCZY721 electrolyte that are difficult to control, as parameters such as sintering temperature and the $Fe_2O_3$/BCZY721 ratio have a profound impact on morphology and the formation of interlacing Ba-rich and Ce-rich phases. As an alternative and promising approach, an iron-filled backbone electrode composed of two consecutively sintered components appears advantageous. This method allows for a significantly lower sintering temperature compared to traditional mixtures, preventing morphological changes and ensuring mechanical stability. Furthermore, sintering the scaffold separately from the pressed in catalyst offers greater flexibility in adjusting parameters and the potential to introduce different catalysts as needed. Even after testing under reducing atmospheres, the cell design, comprising a BCZY721 backbone with inserted iron, demonstrates mechanical stability. The first tests indicate that the electrode design developed is suitable for ammonia production compared to the existing literature, with ammonia formation rates at −1.2 V of $1.1{\cdot}10^{-9}$ mol cm$^{-2}$ s$^{-1}$, $4.9{\cdot}10^{-9}$ mol cm$^{-2}$ s$^{-1}$ and $5.0{\cdot}10^{-9}$ mol cm$^{-2}$ s$^{-1}$ measured at 400 °C, 500 °C and 600 °C for a 12.57 cm$^2$ active electrode area, respectively. This represents the largest active area reported in the literature to date for electrochemical ammonia synthesis using a proton-conducting ceramic membrane.

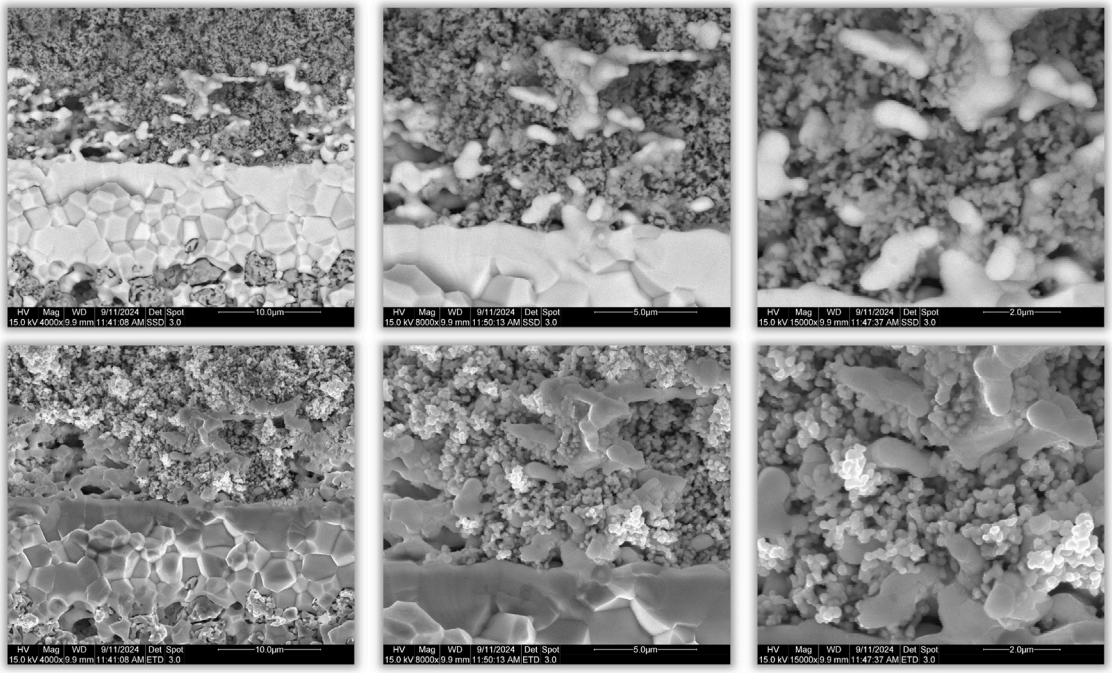

**Fig. 10.** SEM image with BSE (top) and SE (bottom) detector of an $Fe_2O_3$-ink (dark phase) pressed into a backbone (bright phase) electrode after testing under reducing atmosphere for one week.

## CRediT authorship contribution statement

**Philipp Blanck:** Writing – original draft, Visualization, Validation, Supervision, Methodology, Investigation, Data curation, Conceptualization. **Daniel Schmider:** Writing – review & editing. **Robert J. Kee:** Writing – review & editing. **Julian Dailly:** Writing – review & editing, Supervision. **Olaf Deutschmann:** Writing – review & editing, Supervision, Project administration.

## Declaration of competing interest

The authors declare that they have no known competing financial interests or personal relationships that could have appeared to influence the work reported in this paper.

## Acknowledgments

The authors gratefully acknowledge Laura-Alena Schäfer from IMD-2 Forschungszentrum Jülich GmbH for her assistance with the topographical imaging. This project was funded by the Deutsche Forschungsgemeinschaft (DFG, German Research Foundation) - 460038541 under the NSF-DFG Echem initiative (DE 659/14-1).

## References

[1] World Economic Forum, The net-zero industry tracker 2022 edition: Ammonia industry, 2022, https://www.weforum.org/reports/the-net-zero-industry-tracker/in-full/ammonia-industry. (Accessed 12 October 2024).

[2] IEA, Ammonia technology roadmap: IEA, Paris, license: CC BY 4.0, 2021, https://www.iea.org/reports/ammonia-technology-roadmap. (Accessed 12 October 2024).

[3] K.H. Rouwenhorst, A.G. Van Der Ham, G. Mul, S.R. Kersten, Islanded ammonia power systems: Technology review & conceptual process design, Renew. Sustain. Energy Rev. 114 (2019) 109339, http://dx.doi.org/10.1016/j.rser.2019.109339.

[4] Q. Hu, C. Tian, D. Bao, H. Zhong, X. Zhang, Protonic ceramic electrochemical cells: Opportunities and challenges for ammonia synthesis, Next Energy 4 (2024) 100144, http://dx.doi.org/10.1016/j.nxener.2024.100144.

[5] I.J. McPherson, T. Sudmeier, J. Fellowes, S.C.E. Tsang, Materials for electrochemical ammonia synthesis, Dalton Trans. 48 (5) (2019) 1562–1568, http://dx.doi.org/10.1039/C8DT04019B.

[6] S. Hagen, R. Barfod, R. Fehrmann, C.J.H. Jacobsen, H.T. Teunissen, K. Ståhl, I. Chorkendorff, New efficient catalyst for ammonia synthesis: barium-promoted cobalt on carbon, Chem. Commun. (11) (2002) 1206–1207, http://dx.doi.org/10.1039/b202781j.

[7] J. Sehested, C.J. Jacobsen, E. Törnqvist, S. Rokni, P. Stoltze, Ammonia synthesis over a multipromoted iron catalyst: Extended set of activity measurements, microkinetic model, and hydrogen inhibition, J. Catalysis 188 (1) (1999) 83–89, http://dx.doi.org/10.1006/jcat.1999.2628.

[8] T. Egyházi, J. Scholtz, V.S. Beskov, SEM-EDAX investigations of use-related microstructural changes in an ammonia synthesis catalyst, React. Kinet. Catal. Lett. 24 (1–2) (1984) 1–8, http://dx.doi.org/10.1007/BF02069592.

[9] M. Okazaki, J. Otomo, Iron-based electrode structures for ammonia electrosynthesis cells with proton-conducting ceramic electrolytes, ECS Trans. 109 (13) (2022) 3–12, http://dx.doi.org/10.1149/10913.0003ecst.

[10] C.-I. Li, H. Matsuo, J. Otomo, Effective electrode design and the reaction mechanism for electrochemical promotion of ammonia synthesis using Fe-based electrode catalysts, Sustain. Energy Fuels 5 (1) (2021) 188–198, http://dx.doi.org/10.1039/D0SE01385D.

[11] M. Ouzounidou, A. Skodra, C. Kokkofitis, M. Stoukides, Catalytic and electrocatalytic synthesis of $NH_3$ in a $H^+$ conducting cell by using an industrial Fe catalyst, Solid State Ion. 178 (1–2) (2007) 153–159, http://dx.doi.org/10.1016/j.ssi.2006.11.019.

[12] S. Klinsrisuk, J. Irvine, Electrocatalytic ammonia synthesis via a proton conducting oxide cell with $BaCe_{0.5}Zr_{0.3}y_{0.16}Zn_{0.04}O_{3-\delta}$ electrolyte membrane, Catal. Today 286 (2017) 41–50, http://dx.doi.org/10.1016/j.cattod.2016.06.051.

[13] G. Marnellos, S. Zisekas, M. Stoukides, Synthesis of ammonia at atmospheric pressure with the use of solid state proton conductors, J. Catalysis 193 (1) (2000) 80–87, http://dx.doi.org/10.1006/jcat.2000.2877.

[14] G. Marnellos, M. Stoukides, Ammonia synthesis at atmospheric pressure, Science 282 (5386) (1998) 98–100, http://dx.doi.org/10.1126/science.282.5386.98.

[15] D.S. Yun, J.H. Joo, J.H. Yu, H.C. Yoon, J.-N. Kim, C.-Y. Yoo, Electrochemical ammonia synthesis from steam and nitrogen using proton conducting yttrium doped barium zirconate electrolyte with silver, platinum, and lanthanum strontium cobalt ferrite electrocatalyst, J. Power Sources 284 (2015) 245–251, http://dx.doi.org/10.1016/j.jpowsour.2015.03.002.

[16] E. Vasileiou, V. Kyriakou, I. Garagounis, A. Vourros, M. Stoukides, Ammonia synthesis at atmospheric pressure in a $BaCe_{0.2}Zr_{0.7}Y_{0.1}O_{2.9}$ solid electrolyte cell, Solid State Ion. 275 (2015) 110–116, http://dx.doi.org/10.1016/j.ssi.2015.01.002.

[17] F. Zhang, Q. Yang, B. Pan, R. Xu, H. Wang, G. Ma, Proton conduction in $La_{0.9}Sr_{0.1}Ga_{0.8}Mg_{0.2}O_{3-\alpha}$ ceramic prepared via microemulsion method and its application in ammonia synthesis at atmospheric pressure, Mater. Lett. 61 (19–20) (2007) 4144–4148, http://dx.doi.org/10.1016/j.matlet.2007.01.060.

[18] J. Otomo, N. Noda, F. Kosaka, Electrochemical synthesis of ammonia with proton conducting solid electrolyte fuel cells at intermediate temperatures, ECS Trans. 68 (1) (2015) 2663–2670, http://dx.doi.org/10.1149/06801.2663ecst.

[19] Z.-J. Li, R.-Q. Liu, J.-D. Wang, Y.-H. Xie, F. Yue, Preparation of $BaCe_{0.8}Gd_{0.2}O_{3-\sigma}$ by the citrate method and its application in the synthesis of ammonia at atmospheric pressure, J. Solid State Electrochem. 9 (4) (2005) 201–204, http://dx.doi.org/10.1007/s10008-004-0582-1.

[20] X. Wang, J. Yin, J. Xu, H. Wang, G. Ma, Chemical stability, ionic conductivity of $BaCe_{0.9-x}Zr_xSm_{0.10}O_{3-\alpha}$ and its application to ammonia synthesis at atmospheric pressure, Chin. J. Chem. 29 (6) (2011) 1114–1118, http://dx.doi.org/10.1002/cjoc.201190209.

[21] Z. Li, R. Liu, Y. Xie, S. Feng, J. Wang, A novel method for preparation of doped $Ba_3(Ca_{1.18}Nb_{1.82})O_{9-\delta}$: Application to ammonia synthesis at atmospheric pressure, Solid State Ion. 176 (11–12) (2005) 1063–1066, http://dx.doi.org/10.1016/j.ssi.2005.01.009.

[22] C. Chen, G. Ma, Proton conduction in $BaCe_{1-x}Gd_xO_{3-\alpha}$ at intermediate temperature and its application to synthesis of ammonia at atmospheric pressure, J. Alloys Compd. 485 (1–2) (2009) 69–72, http://dx.doi.org/10.1016/j.jallcom.2009.05.108.

[23] R. Liu, Y. Xie, J. Wang, Z. Li, B. Wang, Synthesis of ammonia at atmospheric pressure with $Ce_{0.8}M_{0.2}O_{2-\delta}$ (M=La, Y, Gd, Sm) and their proton conduction at intermediate temperature, Solid State Ion. 177 (1–2) (2006) 73–76, http://dx.doi.org/10.1016/j.ssi.2005.07.018.

[24] W.B. Wang, X.B. Cao, W.J. Gao, F. Zhang, H.T. Wang, G.L. Ma, Ammonia synthesis at atmospheric pressure using a reactor with thin solid electrolyte $BaCe_{0.85}y_{0.15}O_{3-\alpha}$ membrane, J. Membr. Sci. 360 (1–2) (2010) 397–403, http://dx.doi.org/10.1016/j.memsci.2010.05.038.

[25] Y. Guo, B. Liu, Q. Yang, C. Chen, W. Wang, G. Ma, Preparation via microemulsion method and proton conduction at intermediate-temperature of $BaCe_{1-x}Y_xO_{3-\alpha}$, Electrochem. Commun. 11 (1) (2009) 153–156, http://dx.doi.org/10.1016/j.elecom.2008.10.038.

[26] M. Zhang, J. Xu, G. Ma, Proton conduction in $Ba_xCe_{0.8}Y_{0.2}O_{3-\alpha}$ + 0.04ZnO at intermediate temperatures and its application in ammonia synthesis at atmospheric pressure, J. Mater. Sci. 46 (13) (2011) 4690–4694, http://dx.doi.org/10.1007/s10853-011-5376-0.

[27] Z. Li, R. Liu, J. Wang, Z. Xu, Y. Xie, B. Wang, Preparation of double-doped $BaCeO_3$ and its application in the synthesis of ammonia at atmospheric pressure, Sci. Technol. Adv. Mater. 8 (7–8) (2007) 566–570, http://dx.doi.org/10.1016/j.stam.2007.08.009.

[28] J. Liu, Y. Li, W. Wang, H. Wang, F. Zhang, G. Ma, Proton conduction at intermediate temperature and its application in ammonia synthesis at atmospheric pressure of $BaCe_{1-x}Ca_xO_{3-\alpha}$, J. Mater. Sci. 45 (21) (2010) 5860–5864, http://dx.doi.org/10.1007/s10853-010-4662-6.

[29] Y. Kobayashi, N. Shimoda, Y. Kimura, S. Satokawa, Electrochemical synthesis of ammonia using proton conducting solid electrolyte and Ru-doped $BaCe_{0.9}Y_{0.1}O_{3-\delta}$ electrode catalyst, ECS Trans. 75 (42) (2017) 43–52, http://dx.doi.org/10.1149/07542.0043ecst.

[30] M. Okazaki, J. Otomo, Electrode-supported protonic ceramic electrolysis cells for electrochemically promoted ammonia synthesis at intermediate temperatures, ACS Omega 8 (43) (2023) 40299–40308, http://dx.doi.org/10.1021/acsomega.3c04478.

[31] Y. Yuan, S. Tada, R. Kikuchi, Electrochemically promoted ammonia synthesis on an $Fe/BaZr_{0.8}Y_{0.2}O_{3-\delta}$ catalyst at ambient pressure, Sustain. Energy & Fuels 6 (2) (2022) 458–465, http://dx.doi.org/10.1039/D1SE01712H.

[32] E. Vasileiou, V. Kyriakou, I. Garagounis, A. Vourros, A. Manerbino, W. Coors, M. Stoukides, Electrochemical enhancement of ammonia synthesis in a $BaZr_{0.7}Ce_{0.2}Y_{0.1}O_{2.9}$ solid electrolyte cell, Solid State Ion. 288 (2016) 357–362, http://dx.doi.org/10.1016/j.ssi.2015.12.022.

[33] R. Lan, K.A. Alkhazmi, I.A. Amar, S. Tao, Synthesis of ammonia directly from wet air using new perovskite oxide $La_{0.8}Cs_{0.2}Fe_{0.8}Ni_{0.2}O_{3-\delta}$ as catalyst, Electrochim. Acta 123 (2014) 582–587, http://dx.doi.org/10.1016/j.electacta.2014.01.026.

[34] R. Lan, K.A. Alkhazmi, I.A. Amar, S. Tao, Synthesis of ammonia directly from wet air at intermediate temperature, Appl. Catal. B: Environ. 152–153 (2014) 212–217, http://dx.doi.org/10.1016/j.apcatb.2014.01.037.

[35] R. Lan, K.A. Alkhazmi, I.A. Amar, S. Tao, Synthesis of ammonia directly from wet air using $Sm_{0.6}Ba_{0.4}Fe_{0.8}Cu_{0.2}O_{3-\delta}$ as the catalyst, Faraday Discuss. 182 (2015) 353–363, http://dx.doi.org/10.1039/C5FD00033E.

[36] I.A. Amar, R. Lan, J. Humphreys, S. Tao, Electrochemical synthesis of ammonia from wet nitrogen via a dual-chamber reactor using $La_{0.6}Sr_{0.4}Co_{0.2}Fe_{0.8}O_{3-\delta}$ - $Ce_{0.8}Gd_{0.18}Ca_{0.02}O_{2-\delta}$ composite cathode, Catal. Today 286 (2017) 51–56, http://dx.doi.org/10.1016/j.cattod.2016.09.006.

[37] K. Wang, H. Chen, S.-D. Li, Z. Shao, $Sr_xTi_{0.6}Fe_{0.4}O_{3-\delta}$ (x=1.0, 0.9) catalysts for ammonia synthesis via proton-conducting solid oxide electrolysis cells (PCECs), J. Mater. Chem. A 10 (46) (2022) 24813–24823, http://dx.doi.org/10.1039/d2ta01669a.

[38] I.A. Amar, R. Lan, S. Tao, Synthesis of ammonia directly from wet nitrogen using a redox stable $La_{0.75}Sr_{0.25}Cr_{0.5}Fe_{0.5}O_{3-\delta}$ –$Ce_{0.8}Gd_{0.18}Ca_{0.02}O_{2-\delta}$ composite cathode, RSC Adv 5 (49) (2015) 38977–38983, http://dx.doi.org/10.1039/C5RA00600G.

[39] W. Guo, Y. Li, S.-D. Li, Z. Shao, H. Chen, Ammonia synthesis *via* a protonic ceramic electrolysis cell (PCEC) using $LaCu_{0.1}Fe_{0.9}O_{3-\delta}$ catalyst, J. Mater. Chem. A 12 (2) (2024) 1200–1210, http://dx.doi.org/10.1039/D3TA04559E.

[40] M. Li, B. Hua, W. Wu, L.-C. Wang, Y. Ding, M.M. Welander, R.A. Walker, D. Ding, Activating nano-bulk interplays for sustainable ammonia electrosynthesis, Mater. Today 60 (2022) 31–40, http://dx.doi.org/10.1016/j.mattod.2022.09.011.

[41] M. Okazaki, J. Otomo, Ceria-iron electrocatalysts for ammonia electrosynthesis using protonic ceramic electrolysis cells, Solid State Ion. 414 (2024) 116649, http://dx.doi.org/10.1016/j.ssi.2024.116649.

[42] S. Anelli, A. Baggio, D. Ferrero, D. Schmider, J. Dailly, M. Santarelli, F. Smeacetto, Characterization and testing of glass-ceramic sealants for protonic ceramic electrolysis cells applications, Ceram. Int. 50 (10) (2024) 17520–17531, http://dx.doi.org/10.1016/j.ceramint.2024.02.240.

[43] E. Skúlason, T. Bligaard, S. Gudmundsdóttir, F. Studt, J. Rossmeisl, F. Abild-Pedersen, T. Vegge, H. Jónsson, J.K. Nørskov, A theoretical evaluation of possible transition metal electro-catalysts for $N_2$ reduction, Phys. Chem. Chem. Phys. : PCCP 14 (3) (2012) 1235–1245, http://dx.doi.org/10.1039/c1cp22271f.